Search for the fade out of a collective enhancement of the nuclear level density

S. Komarov,[1,2] R. J. Charity,[1] C. J. Chiara,[1] W. Reviol,[1] D. G. Sarantites,[1] and L. G. Sobotka[1,2]
[1]*Department of Chemistry, Washington University, St. Louis, Missouri 63130, USA*
[2]*Department of Physics, Washington University, St. Louis, Missouri 63130, USA*

A. L. Caraley
Department of Physics, State University of New York at Oswego, New York 13126, USA

M. P. Carpenter and D. Seweryniak
Physics Division, Argonne National Laboratory, Argonne, Illinois 60439, USA
(Received 1 March 2007; published 18 June 2007)

The fade out of a collective enhancement of the nuclear level density is predicted (by an SU3 shell model) to give rise to a clear signature in the evolution of the spectral shape of evaporated charged particles with excitation energy. We have searched for this signature in the spectra of α particles emitted from ^{178}Hf compound nuclei, with excitation energies between 54 and 124 MeV, formed in ^{18}O+^{160}Gd fusion reactions. The Gammasphere spectrometer provided us with the ability to construct channel-specific α-particle spectra that could be compared to statistical-model calculations on a channel-by-channel basis. The expected clear signature of a rapid fade out of a collective enhancement was not found. The data are best reproduced by calculations that do not explicitly consider a collective enhancement and its fade out.

DOI: 10.1103/PhysRevC.75.064611 PACS number(s): 25.70.Gh

I. INTRODUCTION

For spherical nuclei at a fixed angular momentum J and total excitation energy E^*, the many-body level density associated with single-particle excitations [1] is

$$\rho_{\rm intr}(E^*, J) = \frac{2J+1}{\sqrt{8\pi}\sigma^3} e^{-\frac{J(J+1)}{2\sigma^2}} \rho_{\rm intr}(E^*), \tag{1}$$

where $\rho_{\rm intr}(E^*)$ is the level density irrespective of spin, and the dimensionless parameter σ is the spin cutoff factor. The latter, expressed in terms of the statistical temperature T and moment of inertia $I_{\rm stat}$, is

$$\sigma = \sqrt{\frac{I_{\rm stat} T}{\hbar^2}}. \tag{2}$$

For a nucleus with axial symmetry, the level density for a specified spin J (with rotational energy $E_{\rm rot}$ and spin cutoff parameter perpendicular to the symmetry axis $\sigma_\perp$) is obtained by summing over the intrinsic states with specified K, the quantum number representing the projection of nuclear spin onto the symmetry axis [2],

$$\rho(E^*, J) = \sum_{K=-J}^{K} \frac{1}{\sqrt{8\pi}\sigma_\perp} e^{\frac{-K^2}{2\sigma_\perp^2}} \rho(E^* - E_{\rm rot}). \tag{3}$$

As pointed out by Björnholm, Bohr, and Mottelson [2], the level density for an axially deformed nucleus, Eq. (3), exceeds that for a spherical nucleus, Eq. (1), by two factors of the spin cutoff factor, one factor for each allowable rotation axis. (There is an additional difference which results from the fact that the spin cutoff factor for rotation perpendicular to the symmetry axis $\sigma_\perp$ is larger than that for rotation parallel to the symmetry axis $\sigma_\parallel$.) As $\sigma_\perp \sim 11\sqrt{T({\rm MeV})}$ (for rare-earth nuclei), this rotational "enhancement" is roughly a factor of 100 at modest excitation energy.

Ignatyuk's [3] formulation for the total collective enhancement, which has been widely adopted, is

$$\rho(E^*, J) = \rho_{\rm intr}(E^*, J) K_{\rm rot}(E^*), \tag{4}$$

where $K_{\rm rot}(E^*) = K_{\rm vib}(E^*) K_{\rm rot}(E^*)$ is assumed to be factorable into vibrational and rotational contributions. As collective motion can be considered as a coherent superposition of single-particle excitations, this collective enhancement is simply a redistribution of strength, pulling it down from high energy, from where a small deficit from a single-particle estimate will hardly be noticed.

The shell effects responsible for nuclear deformation must disappear with increasing excitation energy. Thus at some excitation energy, the distinction between rotational and intrinsic motions becomes impossible and any collective effect should disappear, $\rho(E, J) \to \rho_{\rm intr}(E, J)$ (i.e., $K_{\rm coll} \to 1$). Björnholm, Bohr, and Mottelson suggested that the statistical temperature at which this happens can be expressed in terms of the mean oscillator frequency ω_0 and the ground-state nuclear quadrupole deformation β_2 [2] as

$$T_{\rm cr} \sim \hbar\omega_0 \beta_2 \sim 40 A^{-1/3} \beta_2 \,{\rm MeV}. \tag{5}$$

Hartree-Fock calculations at finite temperature indicate that the quadrupole and hexadecapole moments of ^{168}Yb diminish with increasing temperature and the nuclear shape becomes almost spherical at $T \sim 3$ MeV [4]. Relativistic Hartree-BCS calculations by Agrawal *et al.* indicate that the thermal evolution of ^{166,170}Er nuclei is marked by the transition from superfluid to the "normal" phase at $T \sim 0.4$ MeV, and the transition from deformed to spherical at $T \sim 2.7$ MeV [5].

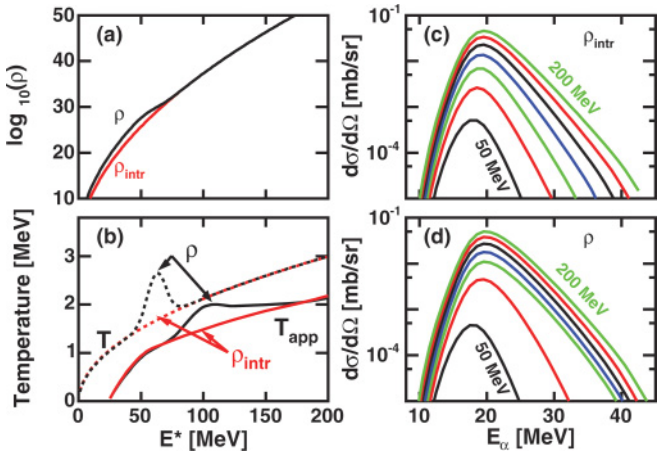

FIG. 1. (Color online) Quantities calculated for ^{168}Yb with two different level density prescriptions. Curves labeled $\rho_{\rm intr}$ are for an intrinsic level density with $a = A/8\,{\rm MeV}^{-1}$; curves labeled ρ are with collective enhancement and fade out following the HJ prescription. (a) level densities, (b) statistical temperatures (dashed), and apparent temperatures from spectra of evaporated α particles $T^{\alpha}_{\rm app}$ (solid). The evolution of the α-particle spectra, for E^* of 50–200 MeV in steps of 25 MeV, are shown in (c) for $a = A/8$ MeV^{-1} and (d) when collective enhancement and fade out are included.

While these works did not directly address the level density, the theoretical study by Hansen and Jensen [6] did.

Within an SU3 shell model, Hansen and Jensen (HJ) extracted a simple prescription for the transition energy and width of the collective enhancement fade out. In this model, both the transition energy $E^*_{\rm cr}$ and the width of the transition region $d_{\rm cr}$ are functions of the ground-state deformation. What is most important for this work is that the transition region for the fade out of the rotational collective enhancement is predicted to occur over a narrow region of excitation energy. If the fade out of the collective enhancement did in fact occur as HJ prescribe, the statistical evaporation spectra would be profoundly affected. This is shown in Fig. 1 and thus illustrates the logic of the present study. Figure 1(a) shows the intrinsic density of states, modeled by $a = A/8$ MeV^{-1}, and the level density, with collective enhancement and its demise, as prescribed by HJ. The statistical temperatures

$$\frac{1}{T} = \frac{d\ln\rho}{dE^*} \tag{6}$$

associated with the intrinsic and collectively enhanced level densities of Fig. 1(a) are shown by the dashed curves in Fig. 1(b). The evolution of the multichance emission spectrum of evaporated α particles with excitation energy is shown in Fig. 1(c) for the case of a fixed level-density constant, while Fig. 1(d) shows this evolution when the enhancement, and its fade out, are modeled by the HJ prescription. Finally, the apparent temperatures $T_{\rm app}$ characterizing the exponential slope of the evaporation spectra are shown in Fig. 1(b), for both cases, as solid curves. The curves for $T_{\rm app}$ are shifted along the E^* axis, relative to those for T, because the apparent temperature reflects the statistical temperature of the average daughter of α-particle emission, while the abscissa is the initial excitation energy of the compound nucleus.

The HJ prescription for the collective enhancement, and its demise, leads to the prediction of an extended plateau of the extracted spectral slope, see curves labeled $T_{\rm app}$ in Fig. 1(b). (In this case, the plateau extends from about 100 to 200 MeV of initial excitation energy.) This work is a search for this extended plateau which, if anything like what is predicted by Hansen and Jensen, would be easily observed. However, our search is tempered by the realization that the HJ model presents a description of an excited nucleus which violates thermodynamic stability. The portion of statistical temperature shown in Fig. 1(b) with negative slope implies a negative heat capacity. This unphysical aspect [7] of the prediction of the demise of a collective enhancement suggests that the transition is likely to be a good deal more gradual than predicted by Hansen and Jensen.

Previously, Junghans *et al.* [8] used the fission survival probability to probe how the level density depends on deformation. The fission rate depends on the density of states of the highly deformed saddle point, while the evaporation residue rate depends on the density of states of the substantially less deformed daughter nuclei. If, for example, the collective enhancements are active for the saddle point and not for the residues of evaporative channels, then fission would be strong and the residue cross section low. This is the expectation if the transition energy, which marks the demise of collective enhancements, were to depend on the "ground-state" deformation of the critical decay configuration. (The critical configuration is the saddle point in the case of fission.) Junghans *et al.* found that this is not supported by the fission survival probability; i.e., statistical-model simulations produce too few residues when the transition energy depends on ground-state deformation [8]. While the data supported a collective enhancement (rotational and vibrational in the case of spherical residues), Junghans *et al.* were forced to use a fade out of the rotational enhancement which was *independent* of the ground-state deformation to reproduce fission survival.

The present work is complementary to that of Junghans *et al.* as the observables are different. The primary result however is, in one respect, similar: the demise of a collective enhancement (to whatever extent it exists) does not manifest itself as predicted by Hansen and Jensen [6]. While the present work places some constraints on the demise of the collective enhancement, the exact form of this transition remains an open question as a clear signature for the predicted transition was not observed.

II. EXPERIMENTAL DETAILS

Excited ^{178}Hf compound nuclei (CN) were created using ^{18}O+^{160}Gd reactions. The ^{18}O nuclei with energies from 79 to 156 MeV were produced by the Argonne National Laboratory ATLAS facility, and the target was isotopically enriched to 98.1%. Table I lists the beam and excitation energies (with the spread in these quantities due to the target thickness, 897 μg/cm^2) and the maximum possible angular momenta for the compound nuclei [9].

TABLE I. Reaction and fitted parameters for the total α-particle spectra.

E_{beam} (MeV)	E^* (MeV)	L_{max} ($\hbar$)	T_{app} (MeV)	B_0 (MeV)	σ_B (MeV)	$d\sigma/d\Omega$ (mb/sr)
78.7 ± 0.8	54.5 ± 0.8	29.7	1.34	14.00	1.43	0.28
84.6 ± 0.8	59.7 ± 0.7	36.9	1.37	14.62	1.58	0.75
90.9 ± 0.8	65.4 ± 0.7	43.2	1.48	14.89	1.62	1.22
100.2 ± 0.7	73.8 ± 0.7	50.8	1.64	15.09	1.64	2.20
108.5 ± 0.7	81.3 ± 0.6	56.6	1.74	15.00	1.64	3.41
116.6 ± 0.7	88.5 ± 0.6	61.5	1.85	15.02	1.67	4.82
126.2 ± 0.6	97.1 ± 0.6	66.3	1.97	15.02	1.67	6.29
135.5 ± 0.6	105.5 ± 0.5	69.9	2.09	15.00	1.67	8.10
145.6 ± 0.6	114.6 ± 0.5	73.5	2.20	14.97	1.68	10.8
156.1 ± 0.5	124.0 ± 0.5	77.1	2.30	14.94	1.75	11.7

The neutron-rich projectile and target were chosen to minimize the fissility parameter $x \sim Z^2/A$ of the CN. GEMINI [10] statistical-model calculations confirm that the fusion-evaporation cross section should be at least an order of magnitude larger than the fusion-fission cross section, see Fig. 2. The validity of these calculations have been verified in a previous experiment for the similar reaction, 159 MeV, $^{18}O+^{154}Sm \rightarrow ^{172}Yb$ [11]. Our choice of systems was also motivated by the requirement that the relevant daughters of evaporation have highly deformed rotating ground states, up to very high spin. The total energy maps, as a function of deformation and spin, generated by Werner and Dudek [12] were used as a guide (to system selection) to fulfill this requirement.

The energy of the evaporated light charged particles was measured with an annular ring counter (RC) located "upstream" of the target, see Fig. 3. This RC is a conventional ΔE-E telescope constructed with a position-sensitive annular 300 μm thick Si detector (ΔE), followed by eight 1.3 mm thick CsI(Tl) scintillation detectors (E). The Si detector has 48 coaxial strip electrodes on one side, and 16 wedge-shaped electrodes on the other. The eight CsI(Tl) E detectors were also wedge shaped. Each wedge-shaped E detector covered 45° in azimuth, matching two of the Si wedge sectors. In the experiment, the RC covered the polar angular range of 150° to 170°. Particle identification was aided by measurements of the particle time of flight t_f as measured by the time difference between the accelerator RF and the Si wedge sectors (triggered by constant-fraction discriminators).

The backward angular region was chosen to protect the RC from elastically scattered beam particles and fission fragments. The backward angle also helps to minimize the contribution from reactions of the beam with light-element contaminants in the target. At forward angles, two small Si detectors were used to monitor the beam and allow the extraction of absolute cross sections.

The linearity of each channel (strips and wedges) of the Si detector was checked with a pulser, and the energy was calibrated with ^{249}Cf and ^{232}U α-particle sources. The mean measured energy resolution for the 8.8 MeV α particles was 45 keV (full width at half maximum). To minimize the effect of charge sharing on the closely spaced annular strips, these strips were only used for the determination of the polar angle, while the wedge electrodes were used for the energy measurement.

The CsI(Tl) energy calibration used the nonlinear form determined by Horn [13]. ^{249}Cf and ^{232}U sources were used to collect α-particle data, while proton data were collected *in situ*, using the proton "punch-through" energies. The measured α-particle energy resolution at 8.8 MeV varied between 4% and 6%. Based on this and beam calibrations of other CsI(Tl) detectors [14], the resolution should be less than 10% in the region of interest (5–40 MeV) with errors in the extrapolated energies (for α particles) of less than 5%.

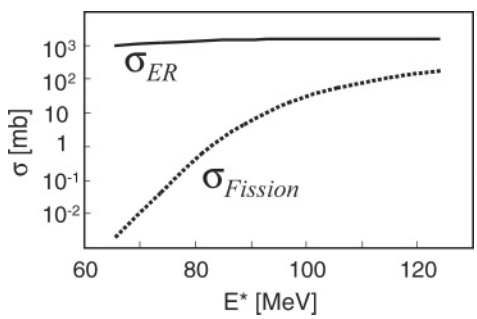

FIG. 2. Statistical-model expectations for fusion-evaporation (solid) and fission (dotted) cross sections as a function of excitation energy.

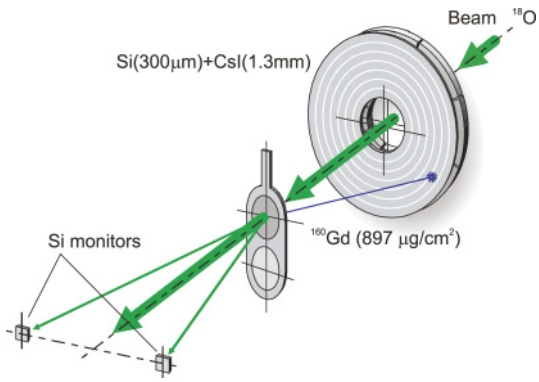

FIG. 3. (Color online) Experimental configuration inside of the Gammasphere vacuum chamber.

The charged-particle apparatus, shown in Fig. 3, was inside Gammasphere, an array of Ge detectors each surrounded by a bismuth germanate (BGO) Compton-suppressor shield [15]. Gammasphere was run without the normal Hevimet absorbers in front of the BGO shields [16]. The absolute photon efficiency (as a function of photon energy E_γ) was obtained by scaling the efficiencies determined by the standard photon-photon procedure to the absolute efficiency at 388 keV determined by taking α-γ coincidence data with a ^{249}Cf source. The ^{249}Cf source data were taken with the same trigger condition as used to collect the beam-generated charged-particle data. These absolute efficiencies peak at 220 keV at a value of 0.19 and drop to 0.09 for 1 MeV photons.

Data were taken at each of the ten energies listed in Table I with both a charged-particle trigger and a Gammasphere trigger. The latter required a minimum of two unsuppressed Ge events. The data from the Gammasphere-triggered runs were used to determine xn excitation functions. The charged-particle trigger was a logical "OR" of the RC with a scaled-down trigger from the forward Si monitors. This allowed the extraction of absolute cross sections for the charged-particle channels by taking a ratio to the Rutherford cross section. Because of constraints in the Gammasphere logic, the (elastic scattering) monitors could not be used for the runs designed to collect data on the xn channels. For these channels, the absolute cross sections were obtained by using the integrated Faraday cup current to normalize between runs with and without the monitors. However, because of human error, this procedure failed for a few beam energies. In these cases, different methods were used to estimate the absolute xn cross sections (see Sec. III E).

The lowest beam energy ($E_{\text{beam}} = 79.6$ MeV) is very near the Coulomb barrier, and therefore all but the smallest impact parameters lead to elastic scattering or Coulomb excitation. Figure 4 shows the ΔE vs time-of-flight maps at both (a) the lowest beam energy and (b) an energy in the middle of the excitation function. The hydrogen and helium loci are clearly identifiable, as is an extra locus of counts, seen only at the lowest beam energy, due to backscattered ^{18}O. Verification of the origin of the latter is made by the prominence of Coulomb-excited target ^{160}Gd lines in the Ge spectra. For the higher beam energies, Coulomb backscattering is negligible.

Figure 4 also shows that the fusion-evaporation protons are not resolved from a region of unidentified particles at low energy and long flight time. The γ-ray spectrum gated on these events has no prominent lines, but some weak lines are tentatively identified as belonging to ^{26}Mg, the residue of the reaction $^{18}\text{O}+^{16}\text{O} \rightarrow {}^{26}\text{Mg} + 2\alpha$. This contamination is very strong for hydrogen and weak for α particles. This work focuses on the cleaner α-particle data. However, even for α particles, generation of clean evaporative spectra (down to low energies) is impossible without some sort of residue gate.

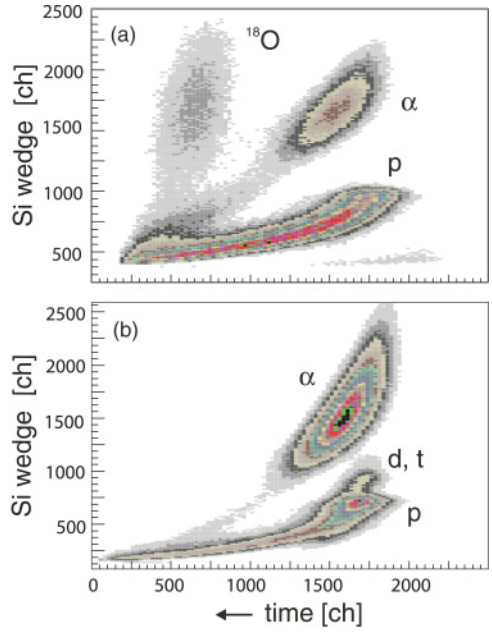

FIG. 4. (Color online) ΔE (Si) vs time-of-flight (Si-RF) maps for $E_{\text{beam}} =$ (a) 79.6 and (b) 117.3 MeV.

III. EXPERIMENTAL DATA

A. Inclusive α-particle spectra

The center-of-mass α-particle spectra are shown in Fig. 5. The upturn at low α-particle energy is a clear indication of a strong admixture of events from reactions on target contaminants. The relative contribution of the contaminant admixture is greatest at low energy, where the α channels of interest have the lowest cross sections. The presence of a significant contaminant contribution in these channel-ungated spectra is also indicated in the high-energy tail of the data at the lowest beam energies.

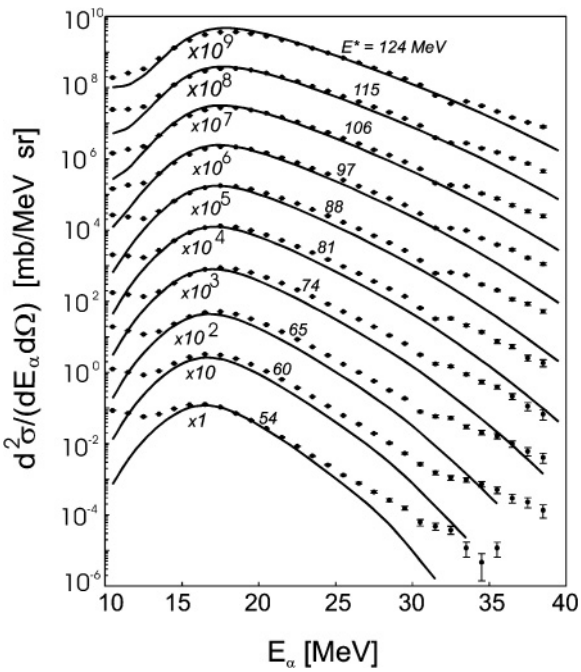

FIG. 5. Ungated α-particle spectra. Scaling powers ($\times 10^N$), are used for display purposes. Only statistical errors are shown. Lines show the results of a statistical-model calculation with $a = A/8$ MeV^{-1} and without the collective enhancement fade out.

The experimental α-particle spectra were fitted to the functional form appropriate for surface emission with a Gaussian distribution of Coulomb barriers [14]:

$$\frac{d^2\sigma}{dE_\alpha d\Omega} = \frac{m}{2(2\pi)^{3/2}T_{\rm app}^2\sigma_B}\int_{-\infty}^{\infty}\chi(E_\alpha - B)(E_\alpha - B) \times \exp\left(-\frac{E_\alpha - B}{T_{\rm app}}\right)\exp\left(-\frac{(B-B_0)^2}{2\sigma_B^2}\right)dB. \quad (7)$$

In this expression, E_α is the α-particle energy in the reaction center of mass, $\chi(E_\alpha)$ is the Heaviside function, B_0 is the mean Coulomb barrier, σ_B is the standard deviation of the barrier distribution, and m is the channel differential multiplicity. The adjustable parameters are, in addition to the normalizing differential multiplicity parameter, the apparent temperature $T_{\rm app}$, mean barrier B_0, and barrier standard deviation σ_B. The low-energy ($E_\alpha < 13$ MeV) and high-energy ($E_\alpha >$ 35 MeV) regions were excluded from the fit. Because the CsI(Tl) detectors have a threshold of ~1 MeV, the α-particle spectra near the Si "punch through" energy are distorted. (See the region at ~31 MeV in the spectra shown in Fig. 5.) This region was also excluded from the fit. The results of the fits to these inclusive spectra are provided in Table I. The fitted parameters have statistical uncertainties of less than 2%.

We use the apparent effective temperature $T_{\rm app}$ as a characteristic parameter to describe not only these spectra, and those generated by channel gating, but also the spectra generated from the statistical-model simulations.

B. γ-ray spectra

The Doppler correction for the xn channels used the velocity appropriate for the residue energy degraded by 1/2 of the target thickness, while the Doppler correction for the charged-particle gated data was made event-by-event, correcting for the recoil of the detected charged particle. The γ-ray transitions in the even-even nuclei were most clearly observed in the spectra, as all decays eventually populate a single ground-state rotational band in these nuclei. This work focuses on these channels.

At the lowest beam energy (corresponding to $E^* =$ 54.5 MeV), the strongest p and α channels are $p4n$ and $\alpha 4n$; while at the highest beam energy ($E^* = 124.0$ MeV), the $p8n$ and $\alpha 8n$ channels have the largest yields. The α-gated γ-ray spectrum at the highest energy is shown in Fig. 6. This is the most complex spectrum (as the number of channels increases with excitation energy, yet the low-lying transitions in the $\alpha 6n$ to $\alpha 10n$ residues can be identified.

C. H-K gates

The standard H (total detected γ-ray energy) vs K (detector fold) procedure [17] was tested as a means both to remove the contaminant contribution and to gate on the compound nucleus spin. The H vs K gates G1, G2, G3, G4, and G5 shown in Fig. 7 were generated for these purposes. The tilting of the gates is intended to compensate for the fact that the angular momentum taken away by statistical γ quanta is, on average, less than that removed by yrast transitions with stretched $E2$ character. The α-particle spectra generated upon application of these gates are shown in Fig. 8. The spectra generated with the G1 gate are strongly contaminated, as evidenced by substantial probability below the expected Coulomb barrier for α-particle emission from rare-earth CN. The same can be said of all gates at the lowest beam energies. The contribution of this contamination in the tails of these $H - K$ gated spectra is uncertain.

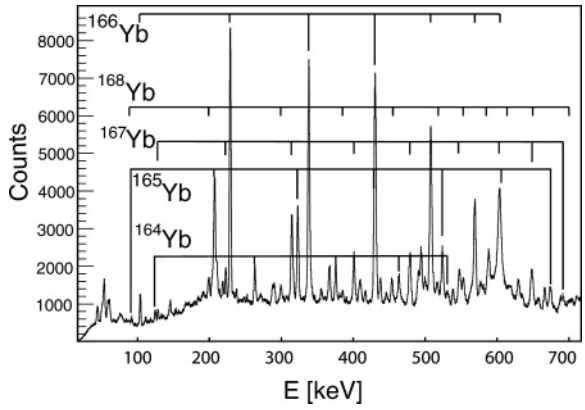

FIG. 6. γ-ray spectrum gated on α-particles for $E_{\rm beam} =$ 156.1 MeV. Lines associated with transitions in the $\alpha 6n$ to $\alpha 10n$ residues are indicated.

$T_{\rm app}(E^*)$ for inclusive and H-K gated data are shown in Fig. 9. As expected, $T_{\rm app}$ increases with E^* in the inclusive data (a) and for each of the gates (b)–(f). In addition, by comparing the trendline for $T_{\rm app}(E^*)$ from the ungated data (which is reproduced in every panel) to the H-K gated data, a decrease in $T_{\rm app}$ with increasing CN spin is clearly seen.

D. αxn channel gating

Channel-gated α spectra were generated for the $\alpha 4n$, $\alpha 6n$, and $\alpha 8n$ channels, corresponding to the even-even nuclei ^{170}Yb, ^{168}Yb, and ^{166}Yb following the procedure used by Westerberg *et al.* [17]. This was done primarily to generate

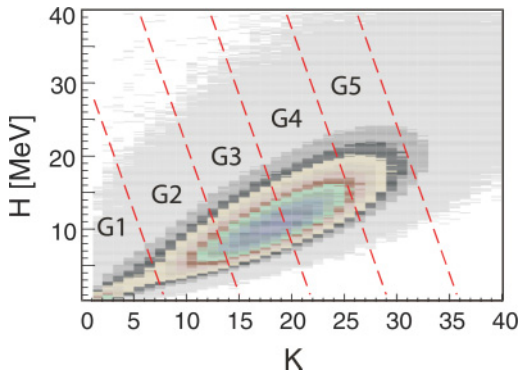

FIG. 7. (Color online) Total H vs K map for $E_{\rm beam} = 156.1$ MeV. Regions G1–G5 represent gates designed to select spin regions.

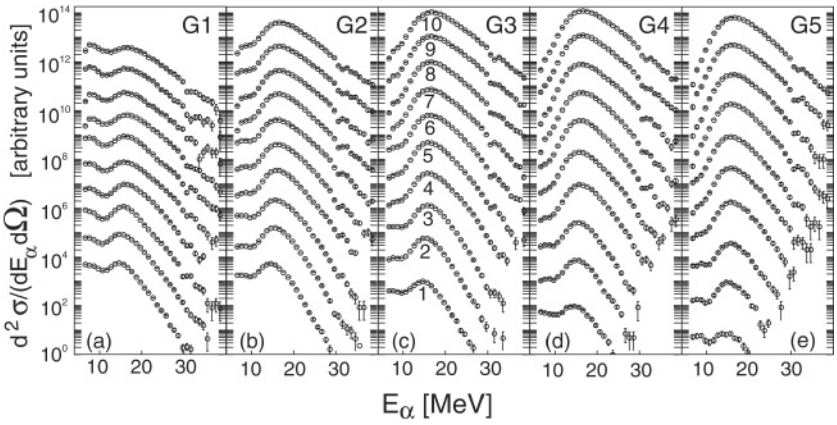

FIG. 8. H-K gated α-particle spectra from gates G1–G5. Spectra labeled 1 through 10 [in (c)] correspond to the beam energies 78.7, 84.6, 90.9, 100.2, 108.5, 116.6, 126.2, 135.5, 145.6, and 156.1 MeV, respectively; see Table I.

spectral shapes free of any contaminant contribution; however, as will be shown below, each channel also provides a coarse angular momentum gate. These channel-gated spectra were built from the coincidence probability of an α particle of a given energy (1 MeV wide bins) and a low-lying γ-ray transition in the selected residue [18]. The γ-ray lines (and channels) employed are

$$228\ \text{keV}\ (4^+ \rightarrow 2^+)\ \text{in}\ ^{166}\text{Yb}\ \alpha 8n,$$
$$299\ \text{keV}\ (6^+ \rightarrow 4^+)\ \text{in}\ ^{168}\text{Yb}\ \alpha 6n,$$
$$193\ \text{keV}\ (4^+ \rightarrow 2^+)\ \text{in}\ ^{170}\text{Yb}\ \alpha 4n,\quad \text{and}$$
$$296\ \text{keV}\ (6^+ \rightarrow 4^+)\ \text{in}\ ^{170}\text{Yb}\ \alpha 4n.$$

The coincidence probabilities were corrected for both internal conversion [19] and the background under the selected transitions. The spectra are displayed in Fig. 10 for the (a) $\alpha 4n$, (b) $\alpha 6n$, and (c) $\alpha 8n$ channels. The low-energy contamination visible in the inclusive spectra is now absent.

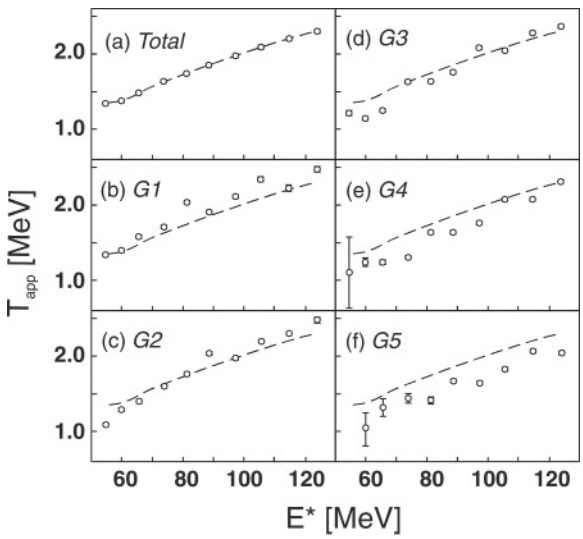

FIG. 9. Apparent temperatures of (a) ungated and (b)–(f) H-K gated α-particle spectra. Dashed trendline for the $T_{\text{app}}(E)$ for the ungated α spectra [from (a)] is reproduced, for reference, in each panel.

These channel-gated α-particle spectra were fitted to Eq. (7), as were the total and H-K gated spectra. The fitting yielded excitation functions for $T_{\text{app}}^{\alpha xn}(E^*)$ and, after correcting for the absolute photon efficiency and integrating over energy and solid angle, excitation functions for the channel cross sections $\sigma^{\alpha xn}(E^*)$. Figure 11 shows the fit values of T_{app}, while Fig. 12 shows the extracted cross sections. The use of the two different transitions for the $\alpha 4n$ channel provides two sets of spectra and thus two sets of $T_{\text{app}}^{\alpha xn}(E^*)$ and $\sigma^{\alpha xn}(E^*)$, see caption. The difference between the two excitation function sets provides a measure of the systematic uncertainty in these quantities based on the photon used for channel selection (i.e. the background, efficiency, and the associated conversion correction associated with the selected photon). The comparison of these experimental $T_{\text{app}}^{\alpha xn}(E^*)$ and $\sigma^{\alpha xn}(E^*)$ excitation functions to statistical-model calculations are made in Sec. V.

Gating on the exit channel itself is another way to coarsely gate on the initial spin of the CN [20,21]. For the same excitation energy, the heaviest residue (fewest evaporated particles) corresponds to compound nuclei with the largest initial angular momentum. For example, from the channel-gated H-K maps shown in Fig. 13, it can seen that the mean detector fold K for the $\alpha 6n$ channel is larger than for the $\alpha 8n$ channel. This indicates that the $\alpha 8n$ residue spin, and likely that of the CN leading to this channel, is smaller than that leading to the $\alpha 6n$ channel.

As the simple H-K gating did not generate contaminant-free, low-spin data, only the channel-gated data are compared with (channel-selected) simulations.

E. Total cross sections for xn channels

The xn channels dominate the reaction yield; thus, the γ rays from these channels dominate the γ-ray spectra taken without the RC trigger. Only at the highest excitation energy can a few weak lines from the charged-particle channel $\alpha 8n$ be identified in the Gammasphere-triggered data. Low-lying transitions from the even-even xn residues were used to estimate the cross section for these channels. The intensities of the following lines were used for the determination of the

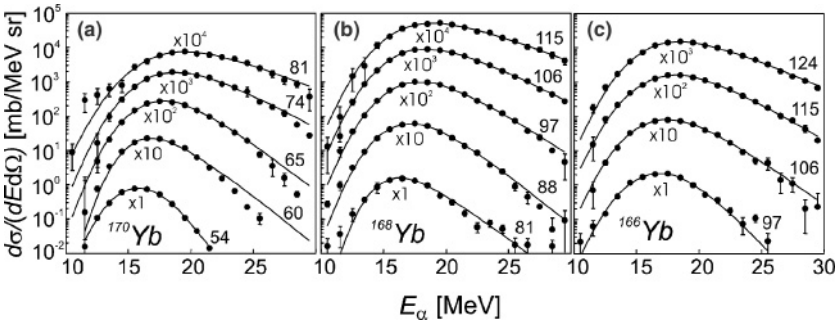

FIG. 10. Channel-gated α-particle spectra obtained from α-γ coincidences for (a) $\alpha 4n$, (b) $\alpha 6n$, and (c) $\alpha 8n$ channels. The fit [to Eq. (7)] spectra are shown as solid lines. The data and fit are labeled by the excitation energy in MeV on the right. Scaling powers ($\times 10^N$) are used for display purposes.

xn cross sections:

$$311\ \text{keV}\ (6^+ \rightarrow 4^+)^{174}\text{Hf}\ 4n,$$
$$214\ \text{keV}\ (4^+ \rightarrow 2^+)^{172}\text{Hf}\ 6n,$$
$$221\ \text{keV}\ (4^+ \rightarrow 2^+)^{170}\text{Hf}\ 8n,\ \text{and}$$
$$262\ \text{keV}\ (4^+ \rightarrow 2^+)^{168}\text{Hf}\ 10n.$$

The intensities of these lines, corrected for conversion and the absolute Gammasphere efficiency, were used along with the Faraday cup integration to estimate the channel cross section. This procedure yielded unphysically high values (due to the aforementioned human error) for the cross sections at $E_{\text{beam}} = 79$, 135, and 156 MeV. For $E_{\text{beam}} > 108$ MeV, the lines corresponding to the $\alpha 6n$ and $\alpha 8n$ channels are seen in the Gammasphere-triggered runs. As a consequence, the cross sections could only be estimated for the xn channels (at these energies) by scaling the yields in these channels to those in the αxn channels, for which the cross sections are known from the RC-triggered runs. (This procedure does not lead to accurate values, as the αxn lines in the Gammasphere-triggered runs are only marginally above background.) As this procedure could not be used at $E_{\text{beam}} = 79$ MeV, the cross sections for the $4n$ and $6n$ channels, at this energy, were inferred by a linear interpolation of the cross section values of these channels at the neighboring beam energies, $E_{\text{beam}} = 85$ and 91 MeV. The experimental total cross sections for xn channels are shown in Fig. 14. The encircled data points required the indirect normalization.

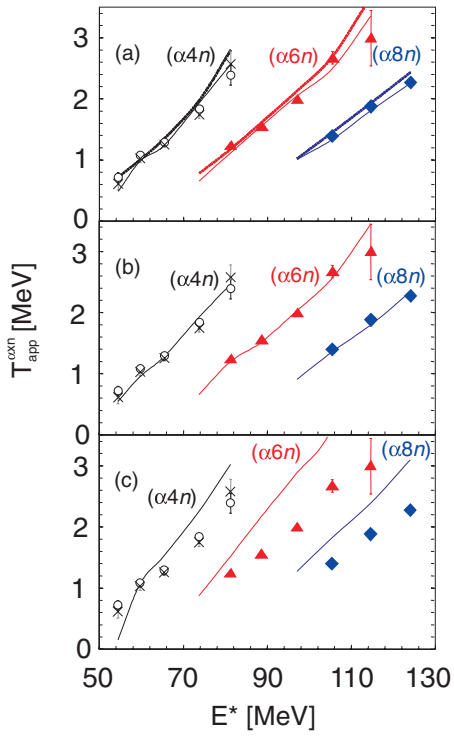

FIG. 11. (Color online) T_{app} for the $\alpha 4n$, $\alpha 6n$, and $\alpha 8n$ channels are shown in all panels as symbols. (Circles and crosses for the $\alpha 4n$ channel result from employing the $6^+ \rightarrow 4^+$ and $4^+ \rightarrow 2^+$ transitions, respectively.) Data are compared with results of GEMINI simulations: (a) without collective enhancement fade out using $\tilde{a} = A/8\ \text{MeV}^{-1}$(solid line) and $A/10\ \text{MeV}^{-1}$ (dotted line); (b) without collective enhancement fade out using a variable level-density parameter $\tilde{a}_{\text{var}}$; and (c) with HJ collective enhancement and fade out using $\tilde{a} = A/8\ \text{MeV}^{-1}$.

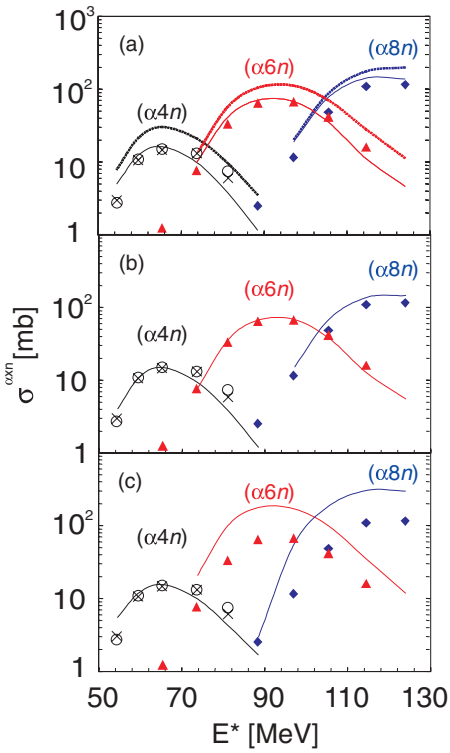

FIG. 12. (Color online) Same as Fig. 11, but showing total cross sections.

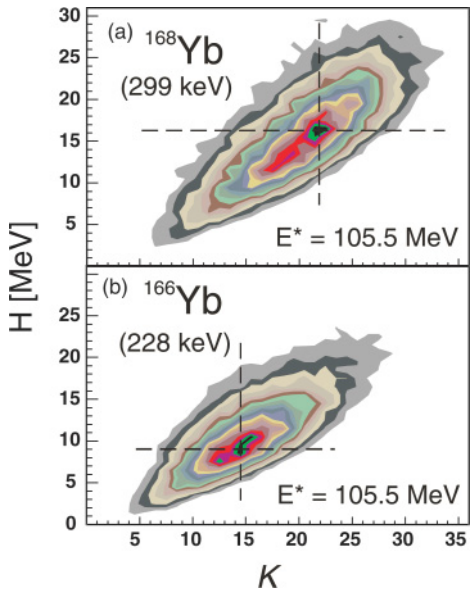

FIG. 13. (Color online) H vs K histograms gated on (a) 299 keV photons from ^{168}Yb ($\alpha 6n$ channel) and (b) 228 keV photons from ^{166}Yb ($\alpha 8n$ channel). The intensity scale is linear.

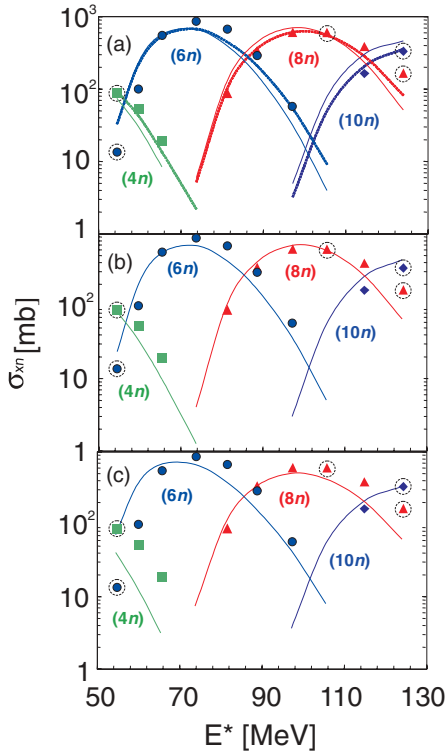

FIG. 14. (Color online) Total cross sections for the $4n$, $6n$, $8n$, and $10n$ channels are shown in all panels as symbols. (Points enclosed in circles are the result of an indirect normalization procedure, see text.) These data are compared with results of GEMINI simulations using (a) no collective enhancement fade out and $\tilde{a} = A/8$ MeV^{-1} (thick line) and $A/10$ MeV^{-1} (thin dotted line); (b) no collective enhancement fade out with $\tilde{a}_{\rm var}$; and (c) with HJ collective enhancement and fade out with $\tilde{a} = A/8$ MeV^{-1}. Experimental data are represented as diamonds for the $10n$, the 226 keV ($4^+ \rightarrow 2^+$) transition in ^{168}Hf; triangles for the $8n$, the 262 keV ($4^+ \rightarrow 2^+$) transition in ^{170}Hf; circles for the $6n$, the 214 keV ($4^+ \rightarrow 2^+$) transition in ^{172}Hf; and squares for the $4n$, the 311 keV ($6^+ \rightarrow 4^+$) transition in ^{174}Hf.

IV. STATISTICAL-MODEL CALCULATIONS

Statistical-model simulations were performed with the Monte Carlo code GEMINI [10]. The transmission coefficients $T_l(E_\alpha)$ are calculated from the ingoing wave boundary condition (IWBC) model [22] using a prescription for the nuclear potential which reproduces the Coulomb barriers in this mass region [14]. Sierk's macroscopic model was used for the calculation of the binding and rotational plus deformation energies as well as fission barriers [23]. A fission delay (of order $\sim 10^{-20}$ s) was adjusted to reproduce the data obtained from a previous ^{18}O+^{144,150,154}Sm experiment [11].

It was assumed that the CN spin distribution follows a rolled-over triangular distribution

$$\frac{d\sigma}{dL} = \frac{\pi \lambda\!\!\!^{-2}(2L+1)}{1+\exp\left(\frac{L-L_{\rm max}}{L_{\rm Diff}}\right)}, \qquad (8)$$

where $\lambda\!\!\!^{-}$ is the entrance-channel reduced deBroglie wavelength, the diffuseness parameter $L_{\rm Diff}$ was set to $2\hbar$, and $L_{\rm max}$ is the maximum angular momentum leading to fusion in the Bass model [9]. The latter was found to be accurate for ^{18}O+^{154,150,144}Sm reactions [11,24].

A. Level-density parameter

To include shell effects, and their washing out with excitation energy, into the statistical calculation, we used an energy-dependent level-density parameter introduced by Ignatyuk [25] and used by many (e.g., Ref. [26]),

$$a(E^*) = \tilde{a}\left\{1+\frac{\delta S}{U}\left[1-\exp\left(-\frac{U}{E_S}\right)\right]\right\}. \qquad (9)$$

$\tilde{a}$ is the asymptotic level-density parameter appropriate for excitation energies above the point where shell effects are washed out. The thermal energy is $U = E^* - E_{\rm rot}$. The damping energy E_S was taken to be 18.5 MeV. The shell energy correction is given by the differences between the experimental and liquid-drop masses $\delta S = M_{\rm exp}(Z,A) - M_{\rm LD}(Z,A,\delta)$. The shell correction energies were less then 1 MeV, and thus their effect on the simulation results (whether present or washed out) is minor.

Simulations were performed using three prescriptions for the asymptotic level-density parameter $\tilde{a}$.

(i) Fixed values of the level-density constant K, i.e., $\tilde{a} = A/K$ with $K = 6$, 8, or 10 MeV.

(ii) The energy-dependent form used in many works [14, 26,27],

$$\tilde{a}_{\rm var}(U) = \frac{A}{K + k^* U/A}. \qquad (10)$$

We used $K = 7$ MeV and $k = 1.3$, values taken from Ref. [14] which are approximately consistent with the calculations of Shlomo and Natowitz [28].

(iii) The prescription proposed by Ignatyuk *et al.* [25], where $\tilde{a}$ is decomposed into volume and surface components $\tilde{a}_{\rm Ign}(A) = 0.073A + 0.095A^{2/3}$ MeV^{-1}. In the mass region of the present study, $\tilde{a}_{\rm Ign}(A) \approx A/11$ MeV^{-1}. (This volume and surface decomposition for the asymptotic level-density parameter $\tilde{a}$ should not be confused with the prescription for including the washing out of shell effects. The prescription for the latter, also from Ignatyuk's work, is used with all prescriptions for $\tilde{a}$.)

For each of these forms, simulations were preformed with one or more forms for the collective enhancement and its fade out.

B. Collective enhancement fade out

The compound nucleus and daughter nuclei formed in the fusion-evaporation reactions of this work are in a region of large ground-state deformations. Their collective motion is predominantly rotational in character; thus, only a collective rotational enhancement is considered, i.e., $K_{\rm vib} = 1$. All level-density prescriptions were simulated *both with and without* the rotational enhancement fade out. Note if there is no fade out, there is very little difference between simulations with and without collective enhancement, as the evaporation spectra are not sensitive to the absolute level density, just its rate of change. As the factor $\sigma_\perp^2(E^*)$ has a small E^* dependence compared to $\rho(E^*)$, the energy dependence of the latter will be the dominant influence on the simulated spectra if rotational enhancement fade out is not included, $K_{\rm rot} = \sigma_\perp^2$.

The rotational enhancement fade out was included in the simulations using a prescription for $K_{\rm rot}(U)$ similar to that employed in Ref. [8]

$$K_{\rm rot}(U) = \begin{cases} (\sigma_\perp^2 - 1)f(U) + 1 & \text{for} \quad \sigma_\perp^2 > 1, \\ 1 & \text{for} \quad \sigma_\perp^2 \leqslant 1. \end{cases} \tag{11}$$

The spin cutoff parameter was evaluated as a function of the quadrupole deformation β_2 using rigid-body moments of inertia $I_\perp = \frac{2}{5} m_0 A R^2 (1 + \beta_2/3)$ with $R = 1.16A^{1/3}$ fm. The ground-state deformations were taken from the calculations of Ref. [29]. Following the suggestion of Hansen and Jensen [6], the damping of the collective enhancement is modeled by a Fermi function

$$f(U) = \frac{1}{1 + \exp[(U - E_{\rm cr})/d_{\rm cr}]},$$

with the dependence of the critical values on β_2 being

$$E_{\rm cr} = 120\beta_2^2 A^{1/3}\ \text{MeV}, \tag{12}$$

$$d_{\rm cr} = 1400\frac{\beta_2^2}{A^{2/3}}\ \text{MeV}. \tag{13}$$

As an example, the $\alpha 6n$ channel leads to the ^{168}Yb residue, for which $\beta_2 = 0.284$, and hence, from Eqs. (12) and (13), $E_{\rm cr} = 53.4$ MeV and $d_{\rm cr} = 3.7$ MeV. Similar values are found for other channels, as the deformation evolves slowly with Z and A. We refer to the calculations with collective enhancement and fade out that use a transition energy and width taken from Eqs. (12) and (13) as calculations using the HJ prescription.

One difference between our implementation of the HJ prescription and that executed in Ref. [8] is that the Fermi function $f(U)$ is now a function of the thermal excitation energy $U = E^* - E_{\rm rot}$ rather than the total excitation energy E^*. This modification was made to account for the high spins induced in the fusion reactions used in the present work.

In principle, the deformation of the appropriate "ground-state configuration" is spin dependent. However, the cranked Strutinsky (macroscopic-microscopic) calculations of Werner and Dudek [12] indicate that both the αxn and xn daughters (both of which are relevant for the statistical-model calculations) maintain the pronounced prolate mimima ($\beta_2 \sim 0.3$) out to between 50 and 60$\hbar$. Therefore, keeping in mind that the relevant equilibrium shape is that of the evaporation daughter (not the CN itself), the use of the ground-state deformation from Ref. [29] to determine the critical parameters is consistent with the HJ prescription throughout most of the range of the excitation function of the present study. On the other hand, conclusions about the HJ prescription for collective enhancement and fade out should not be based solely on the results of the highest energies of the excitation function of this work.

The rotational enhancement coefficients $K_{\rm rot}$, calculated using the HJ prescription, are shown in Fig. 15 for two relevant nuclei. An enhancement of almost a factor of 100 to the level density is predicted to die off between 40 and 60 MeV of excitation energy in the rare-earth nuclei of relevance (the daughters of the α-particle decay).

V. COMPARISON OF STATISTICAL-MODEL SIMULATIONS TO THE DATA

The apparent temperatures extracted from the fits of the total α-particle spectra (Fig. 5) are reproduced in every panel of Fig. 16. These data are compared with GEMINI results using (a) $\tilde{a} = A/8$ and $\tilde{a} = A/10$ MeV^{-1}, (b) $\tilde{a}_{\rm var}$, (c) the HJ collective enhancement prescription with $\tilde{a} = A/8$ MeV^{-1}, and (d) the HJ collective enhancement prescription using $\tilde{a}_{\rm Ign}$ [25].

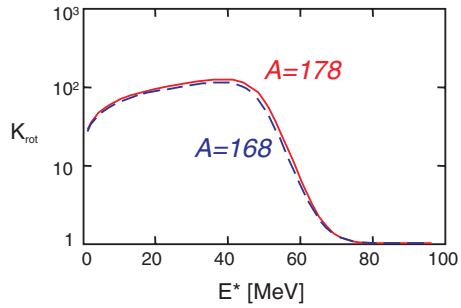

FIG. 15. (Color online) Rotational enhancement coefficient $K_{\rm rot}$ for $A = 178$ (solid) and $A = 168$ (dashed). Ground-state deformation is $\beta = 0.27$.

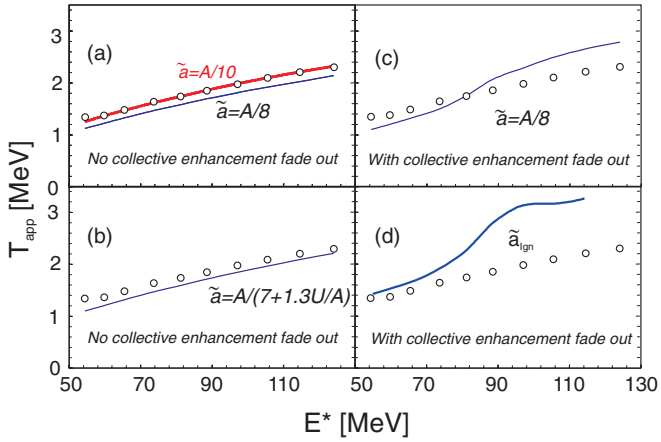

FIG. 16. (Color online) Apparent temperatures of total α-particle spectra. Experimental data (circles) are reproduced in all panels. Lines are the results for the simulations: (a) without collective enhancement fade out and for $\tilde{a} = A/8$ and $A/10$ MeV^{-1}; (b) without collective enhancement and with $\tilde{a}_{\rm var} = A/(7 + 1.3U/A)$ MeV^{-1}; (c) with collective enhancement for $\tilde{a} = A/8$ MeV^{-1}; and (d) with collective enhancement for $\tilde{a}_{\rm lgn}$.

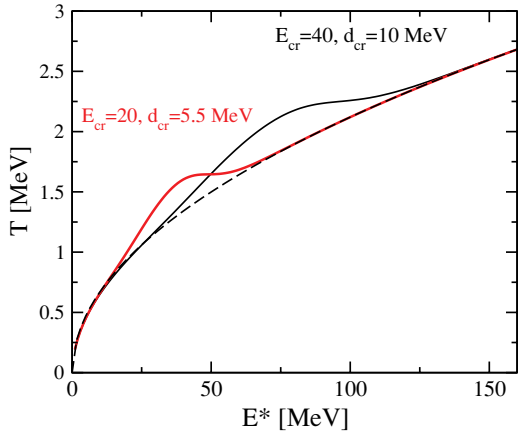

FIG. 17. (Color online) Statistical temperatures (as a function of excitation energy) for $\tilde{a} = A/8$ MeV^{-1} with no collective enhancement and fade out (dashed), and including collective enhancement and fade out with a transition energy of 20 MeV and width of 5.5 MeV (thick solid line) and with a transition energy of 40 MeV and width of 10 MeV (thin solid line).

The simulations using the HJ prescription for the fade out of a collective enhancement [Figs. 16(c) and 16(d)] display a wiggle at $E^* \sim 80$ MeV which is not seen in the data. Needless to say, no wiggle is seen in the temperatures extracted from the simulations without the collective enhancement and fade out, Figs. 16(a) and 16(b). The latter are smooth and continuously increase with excitation energy. Clearly, the simulations are sensitive to a collective enhancement fade out if it were to occur as predicted, and they are not observed as predicted in the $T_{\rm app}$ values extracted from the total spectra.

Calculated values of $T_{\rm app}$ and σ for the αxn channels are compared with the data in Figs. 11 and 12, while Fig. 14 shows the xn channel cross sections. Again, the data are reproduced in each panel and compared with the GEMINI results with (a) $\tilde{a} = A/8$ and $\tilde{a} = A/10$ MeV^{-1} in the top panels, (b) $\tilde{a}_{\rm var}$ in the center panels, and (c) the HJ collective enhancement prescription with $\tilde{a} = A/8$ MeV^{-1} in the bottom panels.

The channel-gated apparent temperatures $T_{\rm app}^{\alpha xn}$ are reasonably well reproduced by either of the fixed level-density constants, $\tilde{a} = A/8$ or $A/10$ MeV^{-1} [Fig. 11(a)], as well as the energy-dependent level-density parameter [14] $\tilde{a}_{\rm var}$ [Fig. 11(b)]. In stark contrast to these cases, the inclusion of the collective enhancement fade-out effect yields apparent temperatures which are too large and increase too quickly with excitation energy [Fig. 11(c)].

The cross sections for the $\alpha 4n$, $\alpha 6n$, and $\alpha 8n$ channels (Fig. 12) are sensitive to the absolute value of $\tilde{a}$. The simulations using $\tilde{a} = A/8$ MeV^{-1} are in somewhat better agreement with the data than are the simulations using $\tilde{a} = A/10$ MeV^{-1} [Fig. 12(a)]. However, use of the energy-dependent prescription $\tilde{a}_{\rm var}$ [14] also reproduces the data reasonably well. Inclusion of a collective enhancement with the HJ fade-out prescription increasingly overshoots the data with increasing excitation energy when a large number of neutrons are removed. [See the $\alpha 8n$ excitation function in Fig. 12(c).]

The xn cross sections, shown in Fig. 14, are less sensitive to the level-density prescriptions than are the αxn cross sections. The inclusion of collective enhancement and fade out with the HJ prescription [Fig. 14(c)] positions the peaks for the $4n$ and $6n$ channels significantly lower in energy than is observed experimentally.

As mentioned in the Introduction, the Hansen and Jensen prescription is suspect from the outset in that it violates thermodynamic stability. Motivated by this and the fact that the HJ prescription produces a clear and unobserved wiggle in the simulated $T_{\rm app}(E^*)$ [see Figs. 16(c) and 16(d)], simulations were also done with two more gradual transitions. The additional sets of values examined are (a) $E_{\rm cr} = 40$ MeV, $d_{\rm cr} = 10$ MeV (transition values used in Ref. [8]) and (b) $E_{\rm cr} = 20$ MeV, $d_{\rm cr} = 5.5$ MeV. The statistical temperatures with these transition parameters never have a negative derivative, see Fig. 17, and thus do not violate thermodynamic stability. (That is, the heat capacity is always positive.)

The cross sections calculated with these more gradual fade-out prescriptions, with $\tilde{a} = A/6$, $A/8$ MeV^{-1}, and $\tilde{a}_{\rm lgn}$ (dashed, solid, and dotted lines, respectively), are compared with experimental data in Fig. 18. As with the HJ prescriptions, these more gradual fade-out forms fail to reproduce the data. For example, with $\tilde{a}_{\rm lgn}$ (dotted lines), the $\alpha 4n$ (and to a lesser extent, the $\alpha 6n$) cross sections are too large. [They exceed the data to such an extent for the lower transition energy that they are not included in Fig. 18(b).] With $\tilde{a} = A/6$, the cross sections are too low for the high-energy end of the $\alpha 4n$ excitation function using either gradual fade-out scheme. The calculations built on $\tilde{a} = A/8$ are the best of these extra cases, but they over estimate the $\alpha 4n$ cross sections and yield $\alpha 8n$ excitation functions which are too steep. Thus, none of the schemes with collective enhancement (and fade out) reproduce the data as well as schemes using either a fixed level-density constant (fixed k in $\tilde{a} = A/k$) or the variable form $\tilde{a}_{\rm var}(U)$ not intended to treat collective enhancements [14].

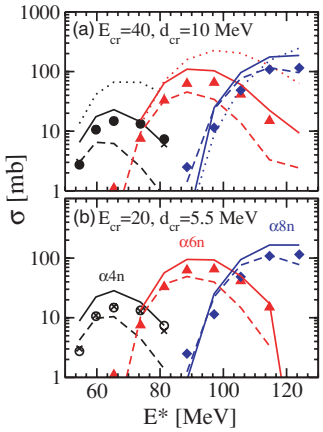

FIG. 18. (Color online) Experimental $\alpha 4n$, $\alpha 6n$, and $\alpha 8n$ cross sections (symbols) are shown in both top and bottom panels. (Circles and crosses for the $\alpha 4n$ channel result from employing the $6^+ \rightarrow 4^+$ and $4^+ \rightarrow 2^+$ transitions, respectively.) Data are compared with statistical model calculations using $\tilde{a} = A/6$ MeV^{-1} (dashed), $\tilde{a} = A/8$ MeV^{-1} (solid), and $\tilde{a}_{\rm lgn}$ (dotted) in (a) with a transition energy of 40 MeV and width of 10 MeV and in (b) with a transition energy of 20 MeV and width of 5.5 MeV. Results for $\tilde{a}_{\rm lgn}$ are omitted in (b) because they predict roughly an order of magnitude too much αxn cross section.

VI. DISCUSSION

While the statistical-model calculations *without* consideration of collective enhancement can provide reasonable reproduction of both the channel-specific excitation functions and the α-particle spectra, consideration of collective enhancements and their fade out using the Hansen and Jensen prescription [6] cannot. Most notably, the latter produces a wiggle in the extracted apparent temperatures that is not found in the data. Moreover, while more gradual transitions cannot be excluded, none of the plausible schemes that were tried reproduced the data as well as those with $\tilde{a} = A/8$ MeV^{-1} or the $\tilde{a}_{\rm var}(U)$ model.

This conclusion is consistent with Junghans *et al.* [8]. They found that the HJ scheme [6] of including the fade out of collective effects is not supported by fission/evaporation residue competition. However, the failure we find is not easily related to that found by Junghans *et al.* The use of fission survival of actinides allowed Junghans *et al.* to test for the influence of collective enhancements at low spin. This removes a considerable complication, which we did not succeed in doing. Furthermore, Junghans *et al.* suggest that the fade out does not depend on (ground-state) deformation, while we find no strong evidence for the fade out at all. However, the Junghans *et al.* result could be related to the fission retardation (delay) issue and perhaps to continuum effects [30]. Furthermore, it is not clear that the HJ prescription for collective enhancement and fade out should pertain to an unstable equilibrium point. The collective enhancement of the ground state is predicted to vanish because the equilibrium shape becomes spherical (at the elevated temperature). It is not at all clear what the relevant unstable equilibrium point (the fission saddle point) should be at elevated temperature. Returning to the major fault of this work, it must be realized that we have tested the HJ logic at moderate to high spin, where it was not intended to be applied. The present study may not have been sensitive to a transition that is broadly spread in spin as well as excitation energy.

VII. CONCLUSIONS

An experiment designed to test for the fade out of a collective enhancement to the level density was performed. The reaction ^{18}O+^{160}Gd $\rightarrow$ ^{178}Hf was used to produce compound nuclei (with highly deformed ground states) with excitation energies between 54 and 124 MeV. Both the α-particle spectra and α and xn channel cross sections were employed. Two procedures were used to generate the α-particle spectra, which are sensitive to the rate of increase of the level density with excitation energy (but not the absolute value), to test for observable consequences of a collective enhancement fade out. These procedures were (1) α-particle spectra generated with H-K gates, in an attempt to isolate specific spin regions (of greatest interest is low spin), and (2) α-particle spectra generated by gating on specific nuclear channels. The low spin H-K gate failed to generate contaminant-free spectra. On the other hand, contaminant-free channel-gated spectra were generated. The channel-gated data provide some measure of spin selection.

Statistical-model simulations were performed with the prescription offered by Hansen and Jensen [6] for the collective enhancement and fade out, two ad-hoc prescriptions to treat the collective enhancement and fade out, as well as several more standard treatments of the level density without any treatment of the collective enhancement and fade out. It is clear from this work that the Hansen and Jensen prescription for the transition is far too sharp. Moreover, we do not find any convincing evidence of the transition at all.

It would be very interesting to compare our experimental results with interacting shell-model Monte Carlo (SMMC) calculations. Although the strict SMMC calculation is applicable only up to $T \sim 1$ MeV, this approach has been extended to higher temperatures using an independent-particle logic but considering both bound and continuum states [31]. This extension allows calculation of level densities up to significantly higher temperatures ($T \sim 4$ MeV). The simulations in Ref. [31] were done for spherical nuclei with $A \sim 50$–70. It would clearly be interesting to apply the same method to heavier nuclei and in particular to deformed nuclei for which collective effects on the level density are expected to be large.

ACKNOWLEDGMENTS

This work was supported by the U.S. Department of Energy, Office of Nuclear Physics, under Grant Nos. DE-FG02-87ER-40316 and DE-FG02-88ER-40406, and Contract No. W31-109-ENG-38.

[1] A. Bohr and B. R. Mottelson, *Nuclear Structure*, Vol. 1 (Benjamin, New York, 1975).
[2] S. Björnholm, A. Bohr, and B. R. Mottelson, in *Proceedings of the International Conference on the Physics and Chemistry of Fission*, Rochester, New York, 1973 (IAEA, Vienna, 1974), Vol. 1, p. 367.
[3] A. V. Ignatyuk, K. K. Istekov, and G. N. Smirenkin, Sov. J. Nucl. Phys. **29**, 450 (1979).
[4] M. Brack and Ph. Quentin, Phys. Scripta A **10**, 163 (1974).
[5] B. K. Agrawal, Tapas Sil, J. N. De, and S. K. Samaddar, Phys. Rev. C **62**, 044307 (2000).
[6] G. Hansen and A. S. Jensen, Nucl. Phys. **A406**, 236 (1983).
[7] R. Lovett, Rep. Prog. Phys. **70**, 195 (2007).
[8] A. R. Junghans, M. de Jong, H.-G. Clerc, A. V. Ignatyuk, G. A. Kudyaev, and K.-H. Schmidt, Nucl. Phys. **A629**, 635 (1998).
[9] R. Bass, Nucl. Phys. **A231**, 45 (1974); Phys. Rev. Lett. **39**, 265 (1977); *Nuclear Reactions with Heavy Ions* (Springer-Verlag, New York, 1980).
[10] R. J. Charity, computer code GEMINI, http://www.chemistry.wustl.edu/~rc.
[11] R. J. Charity, J. F. Dempsey, R. Popelka, and L. G. Sobotka (unpublished).
[12] T. R. Werner and J. Dudek, At. Data Nucl. Data Tables **50**, 179 (1992).
[13] D. Horn, G. C. Ball, A. Galindo-Uribarri, E. Hagberg, R. B. Walker, R. Laforest, and J. Pouliot, Nucl. Instrum. Methods A **320**, 273 (1992).
[14] R. J. Charity, L. G. Sobotka, J. F. Dempsey, M. Devlin, S. Komarov, D. G. Sarantites, A. L. Caraley, R. T. deSouza, W. Loveland, D. Peterson, B. B. Back, C. N. Davids, and D. Seweryniak, Phys. Rev. C **67**, 044611 (2003).
[15] I.-Y. Lee, Nucl. Phys. **A520**, 641c (1990).
[16] M. Devlin, L. G. Sobotka, D. G. Sarantites, and D. R. LaFosse, Nucl. Instrum. Methods A **383**, 506 (1996).
[17] L. Westerberg, D. G. Sarantites, D. C. Hensley, R. A. Dayras, M. L. Halbert, and J. H. Barker, Phys. Rev. C **18**, 796 (1978).
[18] R. B. Firestone and V. S. Shirley, *Table of Isotopes*, 8th ed. (Wiley, New York, 1996).
[19] F. Rösel, H. M. Fries, K. Alder, and H. C. Pauli, At. Data Nucl. Data Tables **21**, 91 (1978).
[20] D. G. Sarantites, M. Jääskeläinen, R. Woodward, F. A. Dilmanian, D. C. Hensley, J. H. Barker, J. R. Beene, M. L. Halbert, and W. T. Milner, Phys. Lett. **B115**, 441 (1982).
[21] M. Jääskeläinen, D. G. Sarantites, R. Woodward, F. A. Dilmanian, J. T. Hood, R. Jääskeläinen, D. C. Hensley, M. L. Halbert, and J. H. Barker, Nucl. Instrum. Methods **204**, 385 (1983).
[22] J. M. Alexander, M. T. Magda, and S. Landowne, Phys. Rev. C **42**, 1092 (1990).
[23] A. J. Sierk, Phys. Rev. C **33**, 2039 (1986).
[24] R. J. Charity, J. R. Leigh, J. J. M. Bokhorst, A. Chatterjee, G. S. Foote, D. J. Hinde, J. O. Newton, S. Ogaza, and D. Ward, Nucl. Phys. **A457**, 441 (1986).
[25] A. V. Ignatyuk, G. N. Smirenkin, and A. S. Tishin, Sov. J. Nucl. Phys. **21**, 255 (1975); A. V. Ignatyuk, M. G. Itkis, V. N. Okolovich, G. N. Smirenkin, and A. S. Tishin, *ibid*. **21**, 612 (1975).
[26] B. J. Fineman, K.-T. Brinkmann, A. L. Caraley, N. Gan, R. L. McGrath, and J. Velkovska, Phys. Rev. C **50**, 1991 (1994).
[27] A. L. Caraley, B. P. Henry, J. P. Lestone, and R. Vandenbosch, Phys. Rev. C **62**, 054612 (2000).
[28] S. Shlomo and J. B. Natowitz, Phys. Rev. C **44**, 2878 (1991).
[29] P. Möller, J. R. Nix, W. D. Myers, and W. J. Swiatecki, At. Data Nucl. Data Tables **59**, 185 (1995).
[30] R. J. Charity and L. G. Sobotka, Phys. Rev. C **71** , 024310 (2005).
[31] Y. Alhassid, G. F. Bertsch, and L. Fang, Phys. Rev. C **68**, 044322 (2003).